IEEE Access
Multidisciplinary | Rapid Review | Open Access Journal

SPECIAL SECTION ON RECONFIGURABLE INTELLIGENT SURFACE AIDED COMMUNICATIONS FOR 6G AND BEYOND

Received July 27, 2021, accepted August 9, 2021, date of publication August 18, 2021, date of current version August 26, 2021.

Digital Object Identifier 10.1109/ACCESS.2021.3105477

Analytical Performance Assessment of Beamforming Efficiency in Reconfigurable Intelligent Surface-Aided Links

GIORGOS STRATIDAKIS, (Graduate Student Member, IEEE), SOTIRIS DROULIAS, AND ANGELIKI ALEXIOU, (Member, IEEE)
Department of Digital Systems, University of Piraeus, 18534 Piraeus, Greece

Corresponding authors: Giorgos Stratidakis (giostrat@unipi.gr) and Sotiris Droulias (sdroulias@unipi.gr)

This work was supported by the Artificial Intelligence Aided D-band Network for 5G Long Term Evolution (ARIADNE) Project under Agreement 871464.

ABSTRACT Future wireless networks designed to operate in the millimeter-wave and terahertz bands are expected to be highly assisted by Reconfigurable Intelligent Surfaces (RIS). The role of the RIS will be to mediate possible non-line-of-sight link by redirecting the incident beam from the transmitter to the receiver and possibly modifying its characteristics, in order to optimize the beamforming efficiency and to maximize the signal power at the receiver. Therefore, it is crucial to understand what are the bounds imposed on the received power and how these bounds depend on the system design parameters. In this paper we show that, contrary to typical line-of-sight links, the increase of the transmitter gain does not always guarantee power increase at the receiver, even for an infinitely large RIS, and we explain how the RIS size can further affect the received power. We present an analytical model that captures the performance of the RIS-aided link in the limit of very large RIS, and we demonstrate numerical examples that provide insight on the interplay between the RIS size and the properties of the transmitter beam.

INDEX TERMS Beamforming efficiency, beam steering, reconfigurable intelligent surface, THz communications.

I. INTRODUCTION

In recent years, the dramatic increase in demand for high data rates has lead the research towards unallocated high frequency bands such as the millimeter-wave (mmWave) (30-100 GHz) and terahertz (THz) bands (0.1-10 THz) [1]–[5]. However, because with increasing frequency pathloss increases and diffraction becomes stronger [5]–[7], the transmitted signals are expected to be more vulnerable to the presence of obstacles (blockage), as compared to operation in the low GHz, for example. In particular, in [5], the authors show that the losses from the human body (e.g. the user) can reach values of 40 dB or greater at 73.5 GHz, while in [8] they show that the user's hand may induce a mean loss of about 15 dB. Therefore, at such high frequencies it is possible that the line-of-sight (LoS) link is blocked even at relatively short distances (in the order of a few meters), thus limiting the practicality of the mmWave and THz bands to mainly short range and LoS scenarios. In order to expand their use to non-line-of-sight (nLoS) scenarios, the use of RISs has been proposed for both in-door ([9]–[12]) and more general scenarios ([13]–[28]).

In [9] a practical RIS phase shift model is presented, along with the joint optimization of the AP transmit beamforming and the RIS beamforming, in order to minimize the transmit power. In [10] the authors investigate the performance of both indoors and outdoors RIS-aided systems and show that a RIS-aided link can even outperform the equivalent LoS link. The authors in [11] propose two schemes to optimize the channel capacity in indoor mmWave environments. The authors in [12], propose a method for improving the focusing of the transmitted signal, using deep neural networks. In [13], a tutorial on the RIS technology is provided to address challenges, such as the channel estimation, the optimization of the reflection and the deployment of the RISs. The authors of [14] derive the far-field pathloss

The associate editor coordinating the review of this manuscript and approving it for publication was Cunhua Pan.

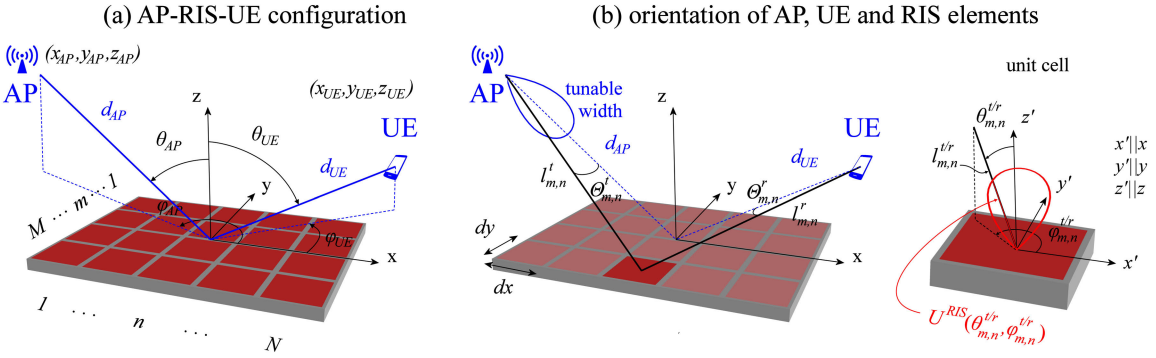

FIGURE 1. System model. (a) Schematic of a RIS-aided link, illustrating the positions and relative angles between the AP, RIS and UE. The RIS consists of $M \times N$ elements (here shown $4 \times 5 = 20$ elements). (b) Details on the orientation of the RIS elements and single unit cell with schematic representation of its radiation pattern. The angle $\Theta^{t}_{m,n}(\Theta^{r}_{m,n})$ denotes the elevation angle from the transmitting (receiving) antenna to the unit cell. The angles $\theta^{t}_{m,n}$, $\phi^{t}_{m,n}$ ($\theta^{r}_{m,n}$, $\phi^{r}_{m,n}$) denote the elevation and azimuth angles from the unit cell to the transmitting (receiving) antenna. Along the designated direction, the normalized power radiation pattern of the unit cell, U^{RIS}, acquires the value $U^{RIS}(\theta^{t/r}_{m,n}, \phi^{t/r}_{m,n})$.

expression for a RIS-aided scenario with the use of physical optics. In [15], the authors develop a general formula to describe the free-space pathloss in RIS-aided systems. Furthermore, they propose three free-space pathloss models for individual scenarios and validate them with experiments. In [16], the authors explore the similarities and differences between relays and RISs that function as anomalous reflectors. Their study shows that RISs of sufficiently large size reduce the complexity of the implementation, while surpassing the relays in terms of data rate. In [17] the authors propose a phase shift design for large intelligent surfaces and evaluate their performance in terms of ergodic spectral efficiency. Furthermore, in [18], the optimization of the data rate and energy efficiency of a RIS-aided multi-user downlink multiple input single output (MIMO) system is performed with two algorithms for the values of the RIS reflectors and the transmit power allocation of the access point (AP). In [19], the coverage probability in the form of a closed-form expression is derived for RIS-aided THz wireless systems. In [20] and [21], the optimal position of the RIS is determined with the prospect of maximizing the signal-to-noise-ratio (SNR) at the receiver. The results show that the RIS should ideally be placed closer to the receiver. In [22], the authors optimize the location of the RIS, in order to maximize the sum rate of multiple UEs. The authors in [23] explore the optimization of the number of elements and the phase shifts of the RIS, in order to maximize the data rate, the energy efficiency and their trade-off. The authors in [24] address the problem of joint design of the reflection coefficients of the RIS and the transmit beamforming under proper and improper Gaussian signalling to optimize the data rate at the receiver. Moreover, in [25] the authors explore the optimization of the RIS-AP distance and the orientation of the RIS in order to maximize the received SNR with the help of a coverage maximization algorithm. In [26] the authors present an analytical approach for the characterization of the SNR distribution and its scaling laws as a function of the number of scattering elements. In [27], the improvement of coverage with the help of RIS in the form of an intelligent wall is explored. Furthermore, in [28] the optimization of beamforming on the RIS is studied in order to minimize the transmit power of the AP, while keeping the received power at the user equipment (UE) constant.

In view of the constantly increasing volume of related works, it becomes clear that there are several parameters that need to be taken into account in order to assess the performance of a RIS-aided link. For example, the received power will strongly depend on the positioning of the RIS with respect to the transmitter and receiver, and will be affected by the RIS size and the properties of the transmitter beam. Therefore, there is a need for a simple analytical model that can clarify the crucial bounds imposed by the system design parameters on the link performance. In this work, in an attempt to provide a generalized approach, the efficiency of the RIS beamforming is studied in terms of the received power. The main contributions are summarized as follows.

- The system performance is qualitatively divided into two regimes of operation, with respect to the RIS size relative to the footprint of the transmitter beam on the RIS.
- For relatively small footprint, a simple analytical model is derived, providing insight on the interplay between crucial parameters, such as the positioning of the RIS with respect to the transmitter and receiver, and the properties of the transmitter beam. The model clarifies why the received power does not increase monotonically with increasing gain, but rather acquires a maximum.
- For relatively large footprint, the impact of the RIS size on the maximum received power is demonstrated through simulations.
- The approach followed in this work provides simple guidelines for the algorithmic design of rules for optimized performance.

II. SYSTEM MODEL

A RIS-aided system model is shown in Fig. 1, where the RIS is centered at the origin of the coordinate system and

consists of $M \times N$ elements (unit cells), periodically arranged along the $x-$ and $y-$ axes, with periodicity dx and dy respectively. The AP is located at (x_{AP}, y_{AP}, z_{AP}) and is equipped with a highly directional antenna with tunable beam-width. The AP illuminates the RIS, which subsequently redirects the incident beam to the UE, located at (x_{UE}, y_{UE}, z_{UE}). In this work, misalignment between the AP and RIS or the RIS and UE is not considered, however the results can be directly extended to account for this possibility. The power received by the UE can be calculated using the power density, S_r, at the UE position and the effective aperture of the UE, A_r, as:

$$P_r = S_r A_r \equiv \frac{|E_r|^2}{2Z_o} A_r, \tag{1}$$

where E_r is the electric field at the position of the UE, Z_o is the characteristic impedance of air and $A_r = \frac{G_r \lambda^2}{4\pi}$, with G_r being the antenna gain of the UE and λ the free-space wavelength. The total electric field at the UE position is:

$$E_r = \sum_{m=1}^{M} \sum_{n=1}^{N} E_{m,n}, \tag{2}$$

where the contribution of the (m, n) RIS element to the total electric field is given by [15], [19]:

$$E_{m,n} = \sqrt{2Z_o P_t G_t A_{RIS} G_{RIS}} \frac{\sqrt{U^t U^{RIS,t} U^{RIS,r} U^r}}{4\pi l^t_{m,n} l^r_{m,n}} \times |R_{m,n}| \exp\left(-j\phi_{m,n}\right) \exp\left(-j\frac{2\pi}{\lambda}(l^t_{m,n} + l^r_{m,n})\right). \tag{3}$$

In Eq.(3) P_t, G_t are the transmitted power and antenna gain of the AP, respectively, A_{RIS}, G_{RIS} are the effective aperture and antenna gain of each RIS element, respectively, $l^t_{m,n}$, $l^r_{m,n}$ are the distances between the (m, n) RIS element and the AP and UE, respectively; $R_{m,n} = |R_{m,n}| \exp(-j\phi_{m,n})$ is the complex reflection coefficient introduced by the (m, n) RIS element. The normalized power radiation pattern of the AP, UE and the RIS element is denoted by U^t, U^r and U^{RIS}, respectively. In particular, $U^t \equiv U^t(\Theta^t_{m,n}, \Phi^t_{m,n})$ is the value of U^t along the direction defined by the AP and the (m, n) element, as shown in Fig. (1b), with the AP targeting the center of the RIS (origin of coordinate system). Similarly, $U^r \equiv U^r(\Theta^r_{m,n}, \Phi^r_{m,n})$ is the value of U^r along the direction defined by the UE and the (m, n) element, with the UE also targeting the center of the RIS. Last, $U^{RIS,t/r}$ is the value of U^{RIS} along the direction defined by the positions of the (m, n) element and the AP/UE, as denoted with the superscript t/r, i.e. $U^{RIS,t/r} \equiv U^{RIS}(\theta^{t/r}_{m,n}, \phi^{t/r}_{m,n})$. Because the RIS elements are identical, they all share a common radiation pattern $U^{RIS} = cos^2\theta^{t/r}_{m,n}$, with $\theta^{t/r}_{m,n} \in [0, \pi/2]$ and $\phi^{t/r}_{m,n} \in [0, 2\pi]$ defined with respect to the coordinate system (x', y', z') [see Fig. (1b), right panel]. Note that, although U^{RIS} is common to all RIS elements, the angles $\theta^{t/r}_{m,n}$, $\phi^{t/r}_{m,n}$ change with (m, n) and, therefore, $U^{RIS,t/r}$ depends on the coordinates of each (m, n) element. Last, regarding the phase introduced by the RIS, it should be noted that a RIS design that aims to redirect a beam from the AP to the UE should provide the linear phase gradient given by [15], [19]:

$$\phi_{m,n} = \frac{2\pi}{\lambda}[(\sin\theta_{UE}\cos\phi_{UE} + \sin\theta_{AP}\cos\phi_{AP})x_m + (\sin\theta_{UE}\sin\phi_{UE} + \sin\theta_{AP}\sin\phi_{AP})y_n], \tag{4}$$

where $x_m = m \times d_x, m = 1, \ldots, M$ and $y_n = n \times d_y$, $n = 1, \ldots, N$ are the coordinates of the (m, n) RIS element.

III. RIS ILLUMINATION REGIMES: RIS SIZE VS AP BEAM FOOTPRINT

In a conventional LoS link, the beam travels from the AP directly to the UE with increasing width –due to free-space propagation– and therefore with decreasing power density, which can be further reduced by possible atmospheric absorption and scattering. As a result, for a certain emitted beam power, the narrower the beam-width at the UE, the higher the power density and the more the power that can be received by the UE. However, when an intermediate re-radiating element, such as a RIS, comes into play, this intuitive picture can change entirely. The reason is that the RIS is essentially a secondary antenna; it is driven by the incident field from the AP and is re-emitting a secondary beam (towards the UE), the propagation characteristics of which depend on both the incident power density on the RIS and the illuminated area.

For highly directional antennas, as considered here, the received power will be largely defined by the main lobe of the AP antenna, regardless of the exact radiation pattern, which will depend on the particular design specifications. Therefore, in order to be able to examine a simple analytical model that can capture the overall performance, beyond the antenna's particular characteristics, a convenient way to approximate the main lobe of a generalized AP antenna and to introduce tunability is to consider a Gaussian radiation pattern (see e.g. [29]) of the form $G_t U^t \equiv G_t \exp(-\frac{G_t}{4}\sin^2\Theta^t_{m,n})$, with $\Theta^t_{m,n} \in [0, \pi/2]$ and $\Phi^t_{m,n} \in [0, 2\pi]$ defined with respect to the coordinate system located at (x_{AP}, y_{AP}, z_{AP}) as shown in Fig. (1b), with $m = 1 \ldots M, n = 1 \ldots N$ (see Appendix A for details). With the AP targeting the center of the RIS, the AP gain becomes maximum (equal to G_t) for the (m, n) element located at the origin (where $U_t = 1$).

$$E = \frac{\sqrt{2Z_o \frac{2P_t}{\pi w^2_{RIS}} |R|^2}}{\sqrt{\left(1 - i\frac{z_B}{z_R}\right)\left(1 - i\frac{z_B}{z_R \cos^2\theta_B}\right)}} \exp\left[-\frac{k_0}{2z_R}\left(\frac{x_B^2 + y_B^2}{1 - i\frac{z_B}{z_R}} - \sin^2\theta_B \frac{(x_B\cos\phi_B + y_B\sin\phi_B)^2}{\left(1 - i\frac{z_B}{z_R}\right)\left(1 + i\frac{z_R\cos^2\theta_B}{z_B}\right)}\right) - ik_0\Phi\right] \tag{5}$$

For highly directional beams, this form for the radiation pattern ensures that the total power radiated from the AP remains practically constant upon beam-width change, i.e. $\int\int (P_t/4\pi d^2) G_t U^t dS \approx P_t$, where dS is the elementary surface element of a sphere of radius d centered at the AP.

In this notation, low G_t means a relatively wide AP beam that can illuminate the entire RIS; therefore, the incident power residing beyond the RIS surface cannot be captured by the RIS, leading effectively to power loss. Intuitively, to compensate for the lost power, G_t must be increased, in order to reduce the area of the AP beam-footprint on the RIS and achieve the utilization of the entire AP beam. Simultaneously, the power density of the beam will increase, as now the same incident power will be concentrated in a smaller region on the RIS, and more power is expected to be received by the UE, similarly to what would happen in a LoS link with increasing AP gain. However, a smaller AP footprint will lead the secondary beam (from the RIS to the UE) to undergo stronger spreading in air, subsequently reducing its power density and possibly leading to the opposite result.

From this discussion it becomes apparent that, besides the incident power density, the size of the RIS illuminated area plays a decisive role on the overall performance of the RIS-aided link and, therefore, the trade-off between the RIS size, AP beam-width and AP power density, can lead to unexpected results with respect to the power received by the UE. To study this trade-off, two regimes of operation can be identified with respect to the RIS size. On the one hand, for relatively low G_t, the AP beam illuminates the entire RIS and, therefore, the footprint of the secondary beam does not depend on the AP beam width, rather is determined by the actual area of the RIS (the effective aperture of the RIS is determined by the finite area of the RIS); we refer to this case as *finite RIS regime*. On the other hand, for relatively high G_t, the AP beam illuminates only a portion of the RIS and, therefore, the width of the secondary beam on the RIS is defined entirely by the AP beam footpint, i.e. the actual RIS size does not matter (the effective aperture of the RIS is determined by the AP beam footprint); in this case the AP beam sees an effectively infinite RIS and we refer to this case as *infinite RIS regime*.

IV. INFINITE RIS REGIME

When the entire AP beam is captured by the RIS we can follow an alternative approach to model the RIS-aided link; we can leave aside the discrete nature of the RIS and treat it as a continuous surface, i.e. we can treat the beam as a continuous distribution. The advantage of this approach over the summation given by Eq.(2) is that the electric field at the position of the UE can be expressed in a simple closed form, enabling the derivation of analytical expressions that provide insight to the RIS operation.

The starting point in this approach is to identify the properties of the AP footprint on the RIS. First, a beam of total power P_t illuminates the RIS, as illustrated schematically in Fig. (2a). For a Gaussian beam, as considered here, the

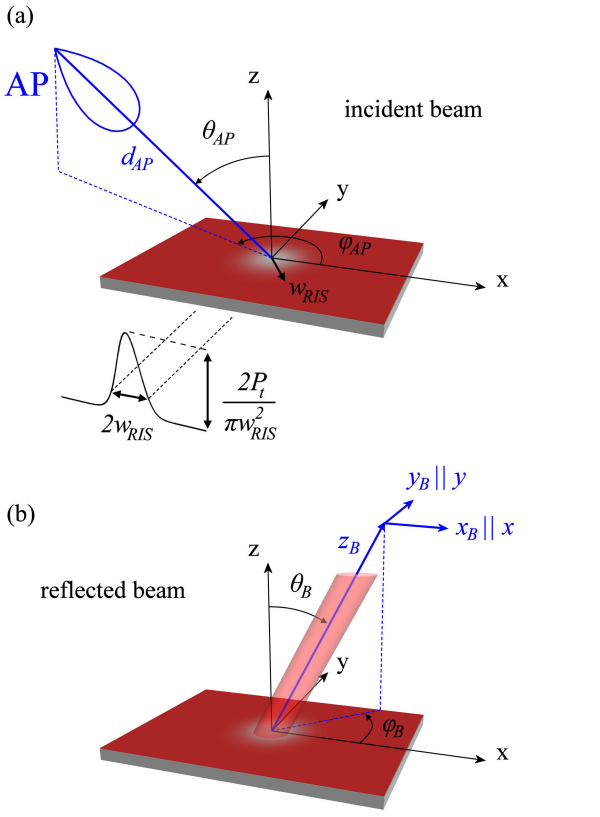

FIGURE 2. Schematic representation of RIS-aided beam steering. (a) The AP illuminates the RIS producing a Gaussian footprint of radius w_{RIS} and peak power density $2P_t/\pi w_{RIS}^2$ [see Eq.(6)]. (b) The incident beam is reflected by the RIS and propagates as a tilted Gaussian beam along the direction defined by the angles θ_B, ϕ_B. The non-orthogonal local beam coordinate system follows the beam as it propagates; z_B is the origin location along the paraxial propagation direction and the transverse coordinates, x_B and y_B, lie on a plane parallel to the x, y- plane.

AP footprint on the RIS is also Gaussian with radius w_{RIS} and power density:

$$S_{RIS}^{inc} = \frac{2P_t}{\pi w_{RIS}^2} \exp\left(-2\frac{x^2+y^2}{w_{RIS}^2}\right). \tag{6}$$

Next, the AP footprint is reflected by the RIS and propagates as a tilted Gaussian beam along the direction defined by the angles θ_B, ϕ_B as shown in Fig. (2b); the non-orthogonal local beam coordinate system follows the beam as it propagates distance z_B from the center of the RIS and the transverse coordinates, x_B and y_B, lie on a plane parallel to the x, y- plane. Due to non-ideal reflection from the RIS, the power density of the reflected beam exactly at the RIS plane is $S_{RIS}^{inc}|R|^2$, where $R \equiv |R_{m,n}|$ is the amplitude of the common reflection coefficient of all RIS elements. Then, following a procedure as in [30], the electric field of the tilted beam produced by such a Gaussian footprint is given by Eq.(5), where z_R is the Rayleigh length, $k_0 = \frac{2\pi}{\lambda}$ is the free-space wavenumber, and:

$$\begin{aligned} x_B &= x - z_B \sin\theta_B \cos\phi_B \\ y_B &= y - z_B \sin\theta_B \sin\phi_B \\ z_B &= z/\cos\theta_B. \end{aligned} \tag{7}$$

The term Φ expresses the phase advance of the redirected beam and is given by: $\Phi = x_B \sin\theta_B \cos\phi_B + y_B \sin\theta_B \sin\phi_B + z_B$. For $\theta_B = \theta_{UE}$, $\phi_B = \phi_{UE}$ the RIS steers the beam towards the UE and, therefore, exactly at the UE position (x_{UE},y_{UE},z_{UE}) where $x_B = 0$, $y_B = 0$ and $z_B = d_{UE}$, the power density at the UE is simply given with the aid of Eq.(5) by:

$$S_r^{inf} = \frac{\frac{2P_t}{\pi w_{RIS}^2}|R|^2}{\sqrt{\left(1+\frac{d_{UE}^2}{z_R^2}\right)\left(1+\frac{d_{UE}^2}{z_R^2\cos^4\theta_{UE}}\right)}}, \tag{8}$$

where the superscript $'inf'$ emphasizes the fact that the result of Eq. (8) derives from the continuous approach in the infinite RIS regime. Then, the power collected by the UE is $P_r^{inf} = S_r^{inf} A_r$, where A_r is the UE effective aperture introduced in Eq. (1).

The denominator of Eq. (8) implies that what is of importance is the RIS-UE distance (d_{UE}) relative to the Rayleigh length z_R, which is a function of w_{RIS} and the wavelength (see Appendix A for details):

$$z_R = \frac{k_0 w_{RIS}^2}{2} \equiv \frac{4k_0 d_{AP}^2}{G_t}. \tag{9}$$

In the limit $d_{UE}/z_R \ll 1$, Eq. (8) acquires a simple form:

$$d_{UE} \ll z_R : P_r^{inf} = A_r|R|^2 \frac{2P_t}{\lambda}\frac{1}{z_R}, \tag{10}$$

i.e. $P_r^{inf} \sim G_t$ [see Eq. (9)], as in typical LoS links. However, in the other extreme:

$$d_{UE} \gg z_R : P_r^{inf} = A_r|R|^2 \frac{2P_t}{\lambda}\frac{\cos^2\theta_{UE}}{d_{UE}^2} z_R, \tag{11}$$

i.e. $P_r^{inf} \sim 1/G_t$, which means that P_r^{inf} decreases with increasing G_t, contrary to what might be intuitively expected, as in the previous case. The two limits imply that there should be a maximum P_r^{inf} for some value of G_t, which can be found by differentiating Eq. (8) with respect to z_R. The maximum power received by the UE is:

$$\max(P_r^{inf}) = A_r|R|^2 \frac{2P_t}{\lambda d_{UE}} \frac{\cos^2\theta_{UE}}{1+\cos^2\theta_{UE}} \tag{12}$$

and occurs when:

$$z_R \cos\theta_{UE} = d_{UE}. \tag{13}$$

Interestingly, the maximum P_r^{inf} does not depend on the position of the AP. This is a direct consequence of the fact that the RIS size is much larger than the AP beam footprint and, hence, the latter can be tuned without limitation. Furthermore, because the Rayleigh length z_R is the distance denoting the transition from the near-field to the far-field of the beam, the result of Eq. (13) dictates that the maximum P_r^{inf} occurs when the UE resides in the vicinity of this transition. In essence, a change in G_t, the gain of the AP, modifies the relative distance z_R with respect to the position of the UE [see Eq. (9)]. By increasing G_t, w_{RIS} decreases, in turn reducing the distance z_R and effectively transferring the UE from the near- to the far-field of the beam. Therefore, relatively low G_t essentially means that $d_{UE} < z_R$ and increasing G_t will increase P_r^{inf} [see Eq.(10)] until the maximum P_r^{inf} is reached [Eq. (12)]. Further increase in G_t will lead to $d_{UE} > z_R$ and to gradual reduction of P_r^{inf} [see Eq.(11)]. The necessary AP gain to reach the maximum P_r^{inf} can be derived from Eq. (13) with the aid of Eq. (9) as:

$$G_t^{inf} = 4k_0 \cos\theta_{UE} \frac{d_{AP}^2}{d_{UE}}. \tag{14}$$

To demonstrate the above, next, a D-band in-door scenario is considered. The operating frequency is 150 GHz and the AP is placed at distance $d_{AP} = 1$ m from the RIS with $\theta_{AP} = 0^o$, while the UE is placed at $d_{UE} = 2$ m with $\theta_{UE} = 20^o$ [see Fig. 1]. The AP, RIS and UE are all on the plane $y = 0$, i.e. $\phi_{AP} = 180^o$ and $\phi_{UE} = 0^o$. The AP transmits a beam of tunable gain, G_t, and constant power $P_t = 1$ W, while the UE gain, G_r, is 20 dB. For a theoretically infinite RIS, the power received by the UE is found using Eq.(8) with the aid of Eq.(9) and is shown in Fig. (3a), as a function of the AP gain, G_t. The equivalent numerical calculation using the discrete model of Eq.(2) is also shown, verifying the theoretically expected power levels. To account for the theoretically infinite RIS in the numerical model, a panel with 1200×1200 elements of size $dx = dy = \lambda/5$ has been considered. For the AP-RIS distance and AP gain levels used in this example, this size is adequate for the RIS to essentially capture the entire AP beam and operate as an effectively infinite panel. In the same Figure, Eq.(10) and Eq.(11) are shown as dashed lines, marking the asymptotic behavior of the communication link in the limit of relatively low and high AP gain. Essentially, the asymptotes serve as an upper threshold for the received power when the link resides in the infinite RIS regime. The vertical dashed line marks the AP gain that provides the maximum power at the UE and is extended to Fig. (3b), to emphasize that this is in agreement with G_t^{inf} as predicted by Eq. (14), which results from the crossing of $z_R \cos\theta_{UE}$ with d_{UE} [graphic solution of Eq.(13)] and marks the transition from the near- to the far- field of the beam.

In Fig. (4) further examples for variable AP and UE positions are presented. In Fig. (4a) the AP is at the position previously examined in Fig. (3) and the UE position is scanned along the direction $\theta_{UE} = 20^o$. For high AP gain ($d_{UE} \gg z_R$) the pathloss increases with increasing d_{UE} and the received power P_r^{inf} decreases, as intuitively expected and also predicted by Eq. (11). For low AP gain ($d_{UE} \ll z_R$), however, the received power is independent of the UE position, as also captured by Eq. (10); this is a direct consequence of the fact that, because the beam propagation is deeply in the near-field, the peak power of the secondary beam is practically constant and the pathloss is therefore similar for all examined cases. Furthermore, with increasing

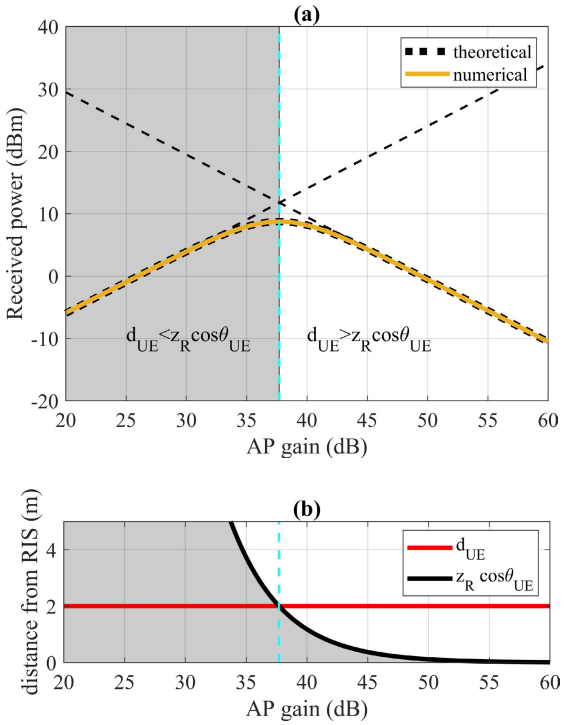

FIGURE 3. RIS-aided link in the infinite RIS regime. (a) Power received by the UE, P_r, as a function of the AP gain, G_t, for an infinitely large RIS (dashed line) and a RIS with $M = N = 1200$ (solid line). (b) Graphic solution of Eq. (13), marking G_t^{inf}, the AP gain that maximizes the received power. The transmitted power is $P_t = 1$ W, the UE gain $G_r = 20$ dB and the AP, RIS and UE lie on the same plane with $d_{AP} = 1$ m, $\theta_{AP} = 0^o$ and $d_{UE} = 2$ m, $\theta_{UE} = 20^o$.

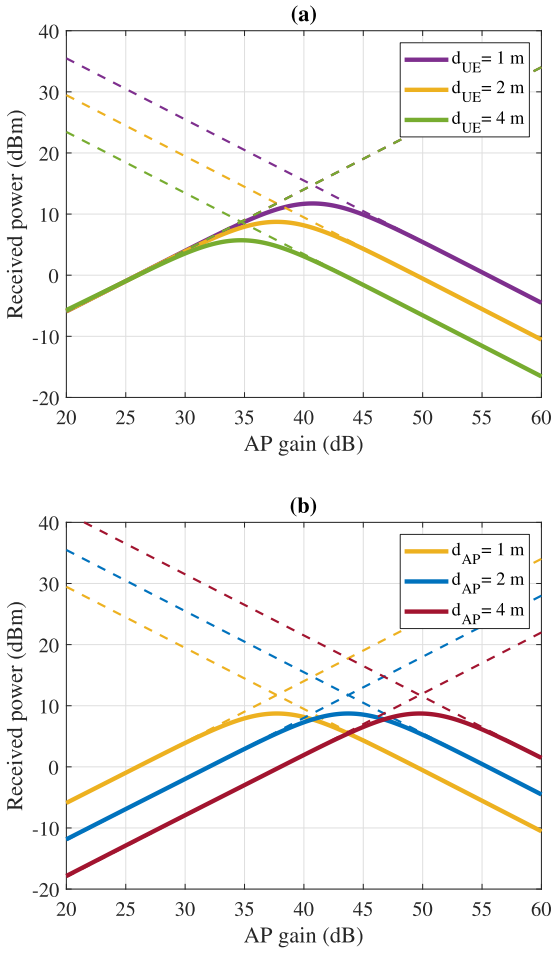

FIGURE 4. Received power, P_r, vs AP gain, G_t, for a RIS-aided link residing in the infinite RIS regime, with a RIS of $M = N = 1200$ elements. (a) Variable RIS-UE distance, d_{UE}, along the direction $\theta_{UE} = 20^o$ with fixed AP position ($d_{AP} = 1$ m, $\theta_{AP} = 0^o$). (b) Variable RIS-AP distance, d_{AP}, along the direction $\theta_{AP} = 0^o$ with fixed UE position ($d_{UE} = 2$ m, $\theta_{UE} = 20^o$). The AP, RIS and UE lie on the same plane, the transmitted power is $P_t = 1$ W and the UE gain is $G_{UE} = 20$ dB.

distance, d_{UE}, the maximum received power drops and moves to lower AP gain, as predicted by Eqs. (12),(14). Physically, this means larger AP footprint, i.e. weaker beam spreading and higher power density at the UE, thus compensating for the increased pathloss at the UE that is placed at larger distances from the RIS. In Fig. (4b) the UE is at the position previously examined in Fig. (3) and the AP position is scanned along the direction $\theta_{AP} = 0^o$. In this case, the maximum received power is independent of the position of the AP [see Eq. (12)] and undergoes a shift towards higher AP gain with increasing d_{AP} [see Eq. (14)]. The reason is that, while an increasing AP-RIS distance leads to an increasing AP footprint and lower power density, with higher AP gain, the same power levels can be restored at a fixed UE position, as demonstrated here. In essence, in the infinite RIS regime, there is always a combination of AP-RIS distance and AP gain that can lead to practically the same power at the UE. This does not hold always, as we will show next, when the finite RIS size comes into play.

V. IMPACT OF FINITE RIS SIZE: FROM PENCIL BEAMS TO WIDE BEAMS AND FULL RIS COVERAGE

Infinitely large RIS does not necessarily imply an actually infinite surface. In practice, it suffices to have a finite-size RIS that is large enough, so that the incident beam is captured entirely by the RIS surface and further increase in the RIS size does not impose any change on the propagation properties of the re-directed beam. Therefore, a direct way to quantify the RIS size is via the percentage of the incident power that is collected by the RIS, as shown in Fig. (5). Clearly, by increasing either the RIS size with fixed AP gain [panel (a)] or the AP gain with fixed RIS size [panel (b)], the power received by the RIS increases until the entire beam is captured. At this limit, the total power captured by the RIS reaches 100% of the incident power and the communication link enters the regime of infinitely large RIS.

To demonstrate the effect of the finite RIS size, the scenario of Fig. (3) is re-examined in Fig. (6) under variable RIS size. Fig. (6a) shows the received power versus the AP gain, G_t, Fig. (6b) shows graphically the solution of Eq.(13) which predicts the AP gain for maximum P_r in the infinite RIS regime and Fig. (6c) shows the transition from the finite to the infinite RIS regime by means of the percentage of the P_t power that is collected by the RIS, as a function of the AP gain. Starting with a large RIS of $M = N = 1200$ elements, the system clearly resides in the infinite RIS regime,

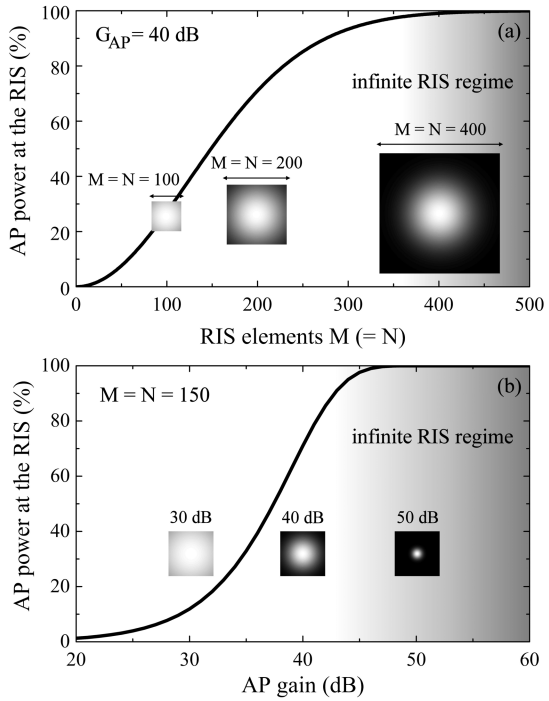

FIGURE 5. Effect of finite RIS size on the AP power received by the RIS. (a) Variable RIS size under constant AP gain (G_{AP} = 40 dB). (b) Variable AP gain under constant RIS size (M = N = 100 elements). The shading denotes that, with increasing AP gain, the communication link gradually enters the infinite RIS regime.

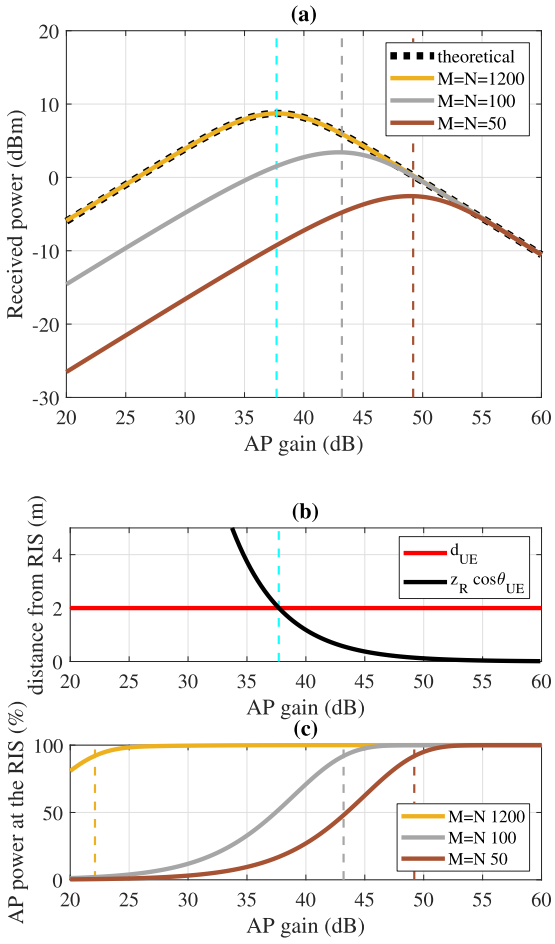

FIGURE 6. Impact of finite RIS size on received power. (a) Received power, P_r, (b) graphic solution of Eq. (13), and (c) power received by the RIS, vs AP gain, G_t, for a RIS with $M = N = 50$, 100 and 1200 elements. The transmitted power is $P_t = 1$ W, the UE gain $G_r = 20$ dB and the AP, RIS and UE lie on the same plane with $d_{AP} = 1$ m, $\theta_{AP} = 0^o$ and $d_{UE} = 2$ m, $\theta_{UE} = 20^o$.

as can be identified in Fig. (6c). As a result, the numerically calculated power shown in Fig. (6a) agrees with the theoretically expected for the infinite RIS, and the maximum received power marked with the cyan dashed line in Fig. (6b) is located at the position predicted by Eqs. (12),(14). With decreasing RIS size the system enters the finite RIS regime as can be identified in Fig. (6c), with implications on the power received by the UE. For low AP gain, the received power decreases with decreasing RIS size [Fig. (6a)], as the amount of P_t captured by the RIS is reduced. For high AP gain, on the other hand, the received power is independent of the RIS size as the footprint of the AP beam on the RIS is always smaller than the RIS size (for the examples considered here) and, therefore, the propagation properties of the secondary beam are not affected by the RIS size. Furthermore, with decreasing RIS size, higher AP gain is required to reach the maximum P_r. This is a direct consequence of the fact that the finite RIS size truncates the incident power and, to compensate for the lost power, the AP footprint must become smaller, so that the entire incident power can be captured by the RIS. Interestingly, the AP gain that restores the power lost due to the finite RIS size is the gain that transfers the system to the infinite RIS regime, i.e. where the power received by the RIS approaches 100% of P_t. Further increase in the AP gain will result in no further power compensation, but to a smaller AP footprint and, therefore, stronger beam spreading and lower power density at the UE.

Last, the example of a UE with variable position - previously studied in Fig. (4a) for an infinitely large RIS- is now examined in Fig. (7) for a small RIS consisting of 80×80 elements. Here, in constrast to the infinitely large RIS case, the received power drops with increasing AP-RIS distance, regardless of the AP gain and the maximum P_r occurs for the same AP gain [panel (a)]. In accordance with the behavior observed in Fig. (6), this is a direct consequence of the fact that, in all cases examined, the theoretically expected AP gain that marks the maximum P_r [panel (b)] is located at lower AP gain levels than the gain that marks the transition from the infinite to the finite RIS regime [panel (c)]. In other words, the power loss from the AP footprint on the RIS due to the finite (relatively small) RIS size dominates, leading to this more intuitive and typical performance.

VI. DISCUSSION

In a communication environment, where the AP beam properties and the RIS operation are tuned according to the UE requirements, there is a need for simple algorithmic

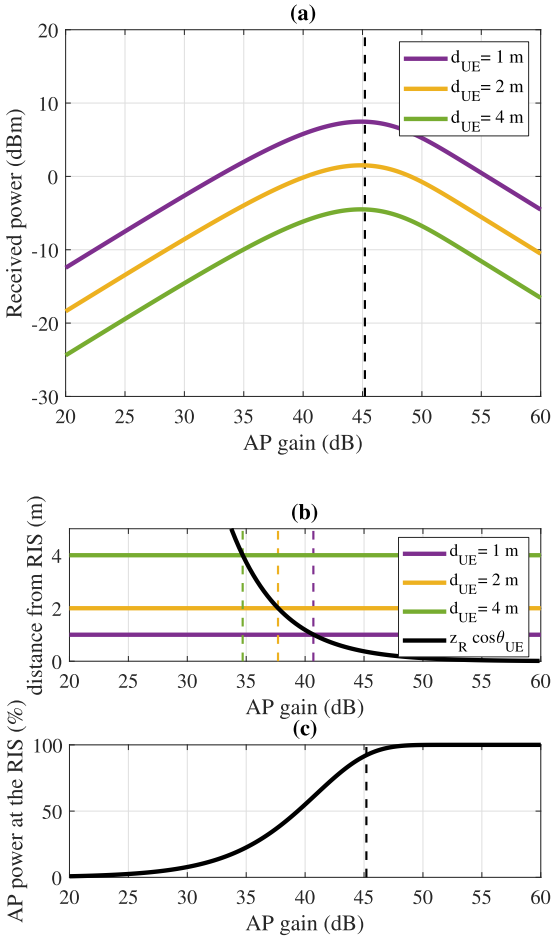

FIGURE 7. RIS-aided link residing in the finite RIS regime, with a RIS of $M = N = 80$ elements. (a) Received power, P_r, (b) graphic solution of Eq. (13), and (c) power received by the RIS, vs AP gain, G_t, for variable UE positions along the direction $\theta_{UE} = 20^o$. The transmitted power is $P_t = 1$ W, the UE gain is $G_{UE} = 20$ dB and the AP, RIS and UE lie on the same plane, with the AP position fixed ($d_{AP} = 1$ m, $\theta_{AP} = 0^o$).

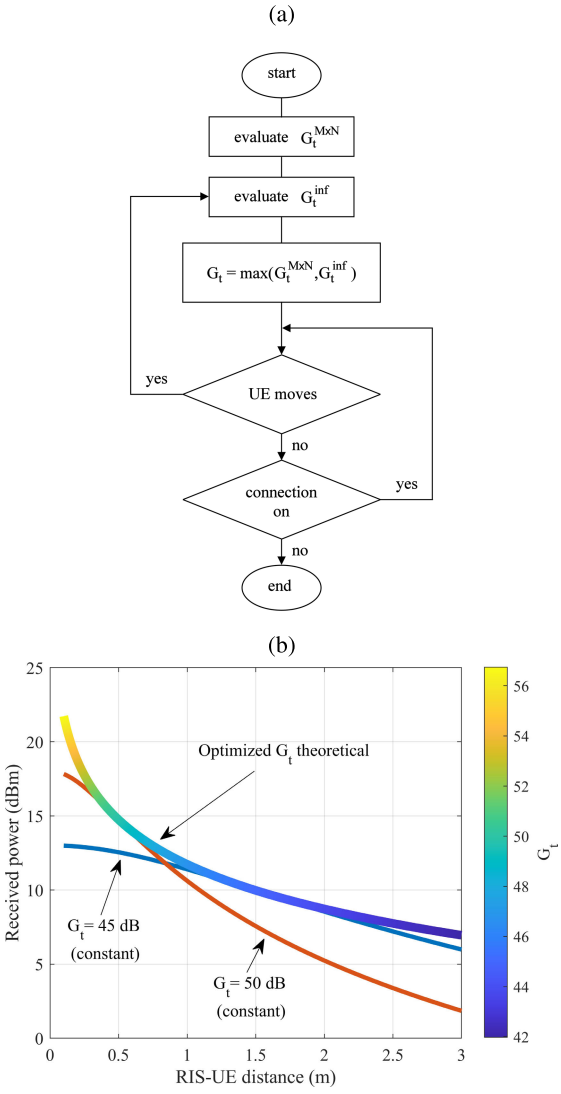

FIGURE 8. Example algorithm for the optimization of the received power at the UE. (a) Flow chart and (b) implementation of algorithm for a RIS of 500 × 500 elements, with the UE moving along the line with $\theta_{UE} = 20^o$ and the AP located at $\theta_{AP} = 0^o$ and $d_{AP} = 2$ m. G_t^{inf} depends on both the AP-RIS and RIS-UE distance and is evaluated when a UE movement is detected. $G_t^{M\times N}$ depends only on the AP-RIS distance and the RIS size and is, therefore, evaluated only once. For comparison, two examples with constant gain are also shown.

description of the possible decisions that have to be made in order to maximize certain key performance indicators (KPIs). With the analysis presented in this work, the dimensionality of the multi-parameter communication space reduces to a few quantities, such as the size of the RIS and the gain of the AP. Then, depending of the KPIs of the particular link, decisions can be made based on these quantities.

For example, in a link where the power received by the UE must be maximized, the entire problem can be expressed in terms of two parameters only, namely G_t^{inf} [given by Eq. (14)] and the gain that marks the transition from the finite to the infinite RIS regime, which we denote here as $G_t^{M\times N}$ (the superscript emphasizes the dependence on the RIS size). From the examples of Fig. (6) and Fig. (7) it becomes apparent that if $G_t^{M\times N} > G_t^{inf}$, then $G_t \equiv G_t^{M\times N}$, while if $G_t^{M\times N} < G_t^{inf}$, then $G_t \equiv G_t^{inf}$. A simple algorithm is shown in the flow chart of Fig. (8a), where $G_t^{M\times N}$ is calculated only once in the beginning and G_t^{inf} is evaluated in real-time, as the UE moves. Another example is when the RIS can be separated in independent blocks, to serve multiple users. In this case $G_t^{M\times N}$ can be calculated a priori for the entire RIS and each block individually, and be compared with G_t^{inf} in a similar manner, as shown in the example of Fig. (8a).

As an implementation of the algorithm shown in Fig. (8a), a scenario of a moving UE is demonstrated in Fig. (8b). As the UE moves, the algorithm decides on the AP antenna gain that optimizes the received power at the UE, leading to an overall stronger reception as compared to the power received under constant AP antenna gain. In this example two cases of constant gain are shown (45 and 50 dB), and the optimized gain for each UE position is shown in the colorbar. The size of the RIS is 500 × 500 elements, the AP is located at $\theta_{AP} = 0^o$ and $d_{AP} = 2$ m, while $\theta_{UE} = 20^o$ and d_{UE} ranges from 0.1 to 3 m.

VII. CONCLUSION

The successful adoption of RISs in future wireless systems is highly dependent on crucial choices for the optimal RIS placement and the efficient transceiver design. In turn, these choices are closely related to certain design parameters that need to be taken into account when designing a RIS-aided link. In this work, the interplay between the RIS size and the properties of the transmitter beam was investigated in terms of the RIS beamforming efficiency. The study revealed that, even for infinitely large RIS, the increase of the transmitter gain does not always guarantee increased power at the receiver, rather there is a maximum, which is further affected by the finite RIS size. The performance of the RIS-aided link was evaluated as a function of the AP gain, revealing two distinct operation regimes, with respect to whether the size of the AP beam footprint is larger or smaller than the RIS area, termed here as *finite RIS regime* and *infinite RIS regime*, respectively. In the infinite RIS regime an analytical model was presented, predicting the maximum received power and providing insight on the underlying mechanism. The theoretically expected performance was also verified by numerical examples of typical in-door scenarios, elucidating the role of variable RIS size, AP-RIS distance and RIS-UE distance.

APPENDIX A

The footprint of the AP beam on the RIS given by Eq. (6), can be written as:

$$S_{RIS}^{inc} = \frac{2P_t}{\pi w_{RIS}^2} U_t, \tag{15}$$

with

$$U_t = \exp\left(-2\frac{x^2+y^2}{w_{RIS}^2}\right) \tag{16}$$

expressing the AP radiation pattern at distance $\sim d_{AP}$, where the RIS is located. The power density of Eq. (15) can be alternatively expressed in terms of G_t, the AP gain, as:

$$S_{RIS}^{inc} = G_t U_t \frac{P_t}{4\pi d^2}, \tag{17}$$

where d is the radius of the sphere centered at the AP, and for pencil beams $d \sim d_{AP}$. From Eq. (15) and Eq. (17) we find:

$$G_t = 8\left(\frac{d_{AP}}{w_{RIS}}\right)^2. \tag{18}$$

The result of Eq. (18) is used in Eq. (9) of the main text, to express z_R in terms of G_t. Additionally, the radiation pattern given by Eq. (16) can be simplified using the result of Eq. (18) and the approximation $\sqrt{x^2+y^2} \sim d_{AP}\sin\theta$, leading to:

$$U_t = \exp\left(-2\frac{d_{AP}^2\sin^2\theta}{w_{RIS}^2}\right) = \exp\left(-\frac{G_t}{4}\sin^2\theta\right), \tag{19}$$

where θ corresponds to the angle $\Theta_{m,n}^t$ shown in Fig.(1) and explained in the relevant text.

REFERENCES

[1] E. N. Papasotiriou, A.-A.-A. Boulogeorgos, A. Stratakou, and A. Alexiou, "Performance evaluation of reconfigurable intelligent surface assisted D-band wireless communication," in *Proc. IEEE 3rd 5G World Forum (5GWF)*, Sep. 2020, pp. 360–365.

[2] A.-A. A. Boulogeorgos, A. Alexiou, T. Merkle, C. Schubert, R. Elschner, A. Katsiotis, P. Stavrianos, D. Kritharidis, P.-K. Chartsias, J. Kokkoniemi, M. Juntti, J. Lehtomaki, A. Teixeira, and F. Rodrigues, "Terahertz technologies to deliver optical network quality of experience in wireless systems beyond 5G," *IEEE Commun. Mag.*, vol. 56, no. 6, pp. 144–151, Jun. 2018.

[3] E. Basar, M. Di Renzo, J. De Rosny, M. Debbah, M. Alouini, and R. Zhang, "Wireless communications through reconfigurable intelligent surfaces," *IEEE Access*, vol. 7, pp. 116753–116773, 2019.

[4] F. F. Manzillo, A. Clemente, and J. L. González-Jiménez, "High-gain D-band transmitarrays in standard PCB technology for beyond-5G communications," *IEEE Trans. Antennas Propag.*, vol. 68, no. 1, pp. 587–592, Jan. 2020.

[5] G. R. MacCartney, S. Deng, S. Sun, and T. S. Rappaport, "Millimeter-wave human blockage at 73 GHz with a simple double knife-edge diffraction model and extension for directional antennas," in *Proc. IEEE 84th Veh. Technol. Conf. (VTC-Fall)*, Sep. 2016, pp. 1–6.

[6] G. Stratidakis, E. N. Papasotiriou, H. Konstantinis, A.-A.-A. Boulogeorgos, and A. Alexiou, "Relay-based blockage and antenna misalignment mitigation in THz wireless communications," in *Proc. 2nd 6G Wireless Summit (6G SUMMIT)*, Mar. 2020, pp. 1–4.

[7] M. Jacob, S. Priebe, R. Dickhoff, T. Kleine-Ostmann, T. Schrader, and T. Kurner, "Diffraction in mm and sub-mm wave indoor propagation channels," *IEEE Trans. Microw. Theory Techn.*, vol. 60, no. 3, pp. 833–844, Mar. 2012.

[8] V. Raghavan, V. Podshivalov, J. Hulten, M. A. Tassoudji, A. Sampath, O. H. Koymen, and J. Li, "Spatio-temporal impact of hand and body blockage for millimeter-wave user equipment design at 28 GHz," *IEEE Commun. Mag.*, vol. 56, no. 12, pp. 46–52, Dec. 2018.

[9] S. Abeywickrama, R. Zhang, Q. Wu, and C. Yuen, "Intelligent reflecting surface: Practical phase shift model and beamforming optimization," *IEEE Trans. Commun.*, vol. 68, no. 9, pp. 5849–5863, Sep. 2020.

[10] I. Yildirim, A. Uyrus, and E. Basar, "Modeling and analysis of reconfigurable intelligent surfaces for indoor and outdoor applications in future wireless networks," *IEEE Trans. Commun.*, vol. 69, no. 2, pp. 1290–1301, Feb. 2021.

[11] N. S. Perovic, M. D. Renzo, and M. F. Flanagan, "Channel capacity optimization using reconfigurable intelligent surfaces in indoor mmWave environments," in *Proc. IEEE Int. Conf. Commun. (ICC)*, Jun. 2020, pp. 1–7.

[12] C. Huang, G. C. Alexandropoulos, C. Yuen, and M. Debbah, "Indoor signal focusing with deep learning designed reconfigurable intelligent surfaces," in *Proc. IEEE 20th Int. Workshop Signal Process. Adv. Wireless Commun. (SPAWC)*, Jul. 2019, pp. 1–5.

[13] Q. Wu, S. Zhang, B. Zheng, C. You, and R. Zhang, "Intelligent reflecting surface-aided wireless communications: A tutorial," *IEEE Trans. Commun.*, vol. 69, no. 5, pp. 3313–3351, May 2021.

[14] O. Özdogan, E. Björnson, and E. G. Larsson, "Intelligent reflecting surfaces: Physics, propagation, and pathloss modeling," *IEEE Wireless Commun. Lett.*, vol. 9, no. 5, pp. 581–585, May 2020.

[15] W. Tang, M. Z. Chen, X. Chen, J. Y. Dai, Y. Han, M. D. Renzo, Y. Zeng, S. Jin, Q. Cheng, and T. J. Cui, "Wireless communications with reconfigurable intelligent surface: Path loss modeling and experimental measurement," *IEEE Trans. Wireless Commun.*, vol. 20, no. 1, pp. 421–439, Jan. 2021.

[16] M. Di Renzo, K. Ntontin, J. Song, F. H. Danufane, X. Qian, F. Lazarakis, J. De Rosny, D.-T. Phan-Huy, O. Simeone, R. Zhang, M. Debbah, G. Lerosey, M. Fink, S. Tretyakov, and S. Shamai, "Reconfigurable intelligent surfaces vs. relaying: Differences, similarities, and performance comparison," *IEEE Open J. Commun. Soc.*, vol. 1, pp. 798–807, 2020.

[17] Y. Han, W. Tang, S. Jin, C. Wen, and X. Ma, "Large intelligent surface-assisted wireless communication exploiting statistical CSI," *IEEE Trans. Veh. Technol.*, vol. 68, no. 8, pp. 8238–8242, Jun. 2019.

[18] C. Huang, A. Zappone, G. C. Alexandropoulos, M. Debbah, and C. Yuen, "Reconfigurable intelligent surfaces for energy efficiency in wireless communication," *IEEE Trans. Wireless Commun.*, vol. 18, no. 8, pp. 4157–4170, Aug. 2019.

[19] A.-A.-A. Boulogeorgos and A. Alexiou, "Coverage analysis of reconfigurable intelligent surface assisted THz wireless systems," *IEEE Open J. Veh. Technol.*, vol. 2, pp. 94–110, 2021.
[20] K. Ntontin, A.-A.-A. Boulogeorgos, D. G. Selimis, F. I. Lazarakis, A. Alexiou, and S. Chatzinotas, "Reconfigurable intelligent surface optimal placement in millimeter-wave networks," *IEEE Open J. Commun. Soc.*, vol. 2, pp. 704–718, 2021.
[21] K. Ntontin, D. Selimis, A.-A.-A. Boulogeorgos, A. Alexandridis, A. Tsolis, V. Vlachodimitropoulos, and F. Lazarakis, "Optimal reconfigurable intelligent surface placement in millimeter-wave communications," in *Proc. 15th Eur. Conf. Antennas Propag. (EuCAP)*, Mar. 2021, pp. 1–5.
[22] Y. Pan, K. Wang, C. Pan, H. Zhu, and J. Wang, "Sum rate maximization for intelligent reflecting surface assisted terahertz communications," 2020, *arXiv:2008.12246*. [Online]. Available: http://arxiv.org/abs/2008.12246
[23] A. Zappone, M. Di Renzo, X. Xi, and M. Debbah, "On the optimal number of reflecting elements for reconfigurable intelligent surfaces," *IEEE Wireless Commun. Lett.*, vol. 10, no. 3, pp. 464–468, Mar. 2021.
[24] H. Yu, H. D. Tuan, A. A. Nasir, T. Q. Duong, and H. V. Poor, "Joint design of reconfigurable intelligent surfaces and transmit beamforming under proper and improper Gaussian signaling," *IEEE J. Sel. Areas Commun.*, vol. 38, no. 11, pp. 2589–2603, Nov. 2020.
[25] S. Zeng, H. Zhang, B. Di, Z. Han, and L. Song, "Reconfigurable intelligent surface (RIS) assisted wireless coverage extension: RIS orientation and location optimization," *IEEE Commun. Lett.*, vol. 25, no. 1, pp. 269–273, Jan. 2021.
[26] X. Qian, M. Di Renzo, J. Liu, A. Kammoun, and M.-S. Alouini, "Beamforming through reconfigurable intelligent surfaces in single-user MIMO systems: SNR distribution and scaling laws in the presence of channel fading and phase noise," *IEEE Wireless Commun. Lett.*, vol. 10, no. 1, pp. 77–81, Jan. 2021.
[27] L. Subrt and P. Pechac, "Controlling propagation environments using intelligent walls," in *Proc. 6th Eur. Conf. Antennas Propag. (EUCAP)*, Mar. 2012, pp. 1–5.
[28] Q. Q. Wu and R. Zhang, "Beamforming optimization for wireless network aided by intelligent reflecting surface with discrete phase shifts," *IEEE Trans. Commun.*, vol. 68, no. 3, pp. 1838–1851, May 2020.
[29] A. Kazemipour, M. Hudlička, R. Dickhoff, M. Salhi, T. Keline-Ostmann, and T. Schrader, "The horn antenna as Gaussian source in the mm-wave domain," *J. Infr., Millim., Terahertz Waves*, vol. 35, no. 9, pp. 720–731, Sep. 2014.
[30] Y. Hadad and T. Melamed, "Non-orthogonal domain parabolic equation and its tilted Gaussian beam solutions," *IEEE Trans. Antennas Propag.*, vol. 58, no. 4, pp. 1164–1172, Apr. 2010.

GIORGOS STRATIDAKIS (Graduate Student Member, IEEE) was born in Athens, Greece, in 1990. He received the bachelor's degree in telecommunications engineering from the Department of Telecommunications Science and Technology, University of Peloponnese, in 2016, and the master's degree in digital communications and networks from the Department of Digital Systems, University of Piraeus, in 2018. He is currently pursuing the Ph.D. degree in wireless communications. He joined the Department of Digital Systems, University of Piraeus, in 2017, where he conducts research in the area of wireless communications.

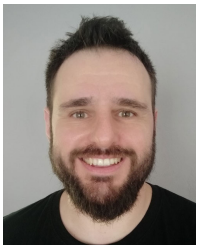

SOTIRIS DROULIAS received the Diploma degree in electrical and computer engineering and the Ph.D. degree in nonlinear photonics from the National Technical University of Athens, Athens, Greece, in 2001 and 2007, respectively. From 2009 to 2012, he worked as an Adjunct Lecturer with the University of Patras. From 2012 to 2020, he was a member of the Photonic- Phononic- and Meta- Materials Group, FORTH-IESL, Crete, Greece. He is currently a Research Associate with the Department of Digital Systems, ICT School, University of Piraeus, Piraeus, Greece. He has worked on several EC funded projects. He is the author of more than 30 articles and two book chapters. His research interests include metamaterials, photonic crystals, metasurfaces, nanolasers, plasmonics, and active media. He has received more than 15 talk invitations in prestigious conferences. He serves as a reviewer in several scientific journals. He received the Best Poster Award for his work on metasurface lasers in META 2019, Lisbon, Portugal, in 2019, and he was recognized as an Outstanding Reviewer from the Institute of Physics (IOP), in 2020.

ANGELIKI ALEXIOU (Member, IEEE) received the Diploma degree in electrical and computer engineering from the National Technical University of Athens, in 1994, and the Ph.D. degree in electrical engineering from Imperial College of Science, Technology and Medicine, University of London, in 2000. Since May 2009, she has been a Faculty Member with the Department of Digital Systems, where she conducts research and teaches undergraduate and postgraduate courses in broadband communications and advanced wireless technologies. Prior to this appointment, she was with Bell Laboratories, Wireless Research, Lucent Technologies, (later Alcatel-Lucent, now NOKIA), Swindon, U.K., first as a member of Technical Staff (from January 1999 to February 2006) and later as a Technical Manager (from March 2006 to April 2009). She is currently a Professor with the Department of Digital Systems, ICT School, University of Piraeus. She is the Project Coordinator of the H2020 TERRANOVA Project (ict-terranova.eu) and the Technical Manager of H2020 ARIADNE Project (ict-ariadne.eu). Her research interests include radio interface for systems beyond 5G, MIMO, THz wireless technologies and reconfigurable intelligent surfaces, efficient resource management for ultra dense wireless networks, machine-to-machine communications, and artificial intelligence and machine learning for future wireless systems. She is a member of the Technical Chamber of Greece. She was a co-recipient of Bell Labs President's Gold Award, in 2002, for contributions to Bell Labs Layered Space-Time (BLAST) project and the Central Bell Labs Teamwork Award, in 2004, for role model teamwork and technical achievements in the IST FITNESS Project. She is the Chair of the Working Group on Radio Communication Technologies and the Working Group on High Frequencies Radio Technologies of the Wireless World Research Forum.